Branch/mode competition in the flow-induced vibration of a square cylinder

Jisheng Zhao, Andras Nemes, David Lo Jacono, John Sheridan

Branch/mode competition in the flow-induced vibration of a square cylinder

Jisheng Zhao[1], András Nemes[1], David Lo Jacono[2] and John Sheridan[1]

[1]Fluids Laboratory for Aeronautical and Industrial Research (FLAIR), Department of Mechanical and Aerospace Engineering, Monash University, Victoria 3800, Australia

[2]Institut de Mécanique des Fluides de Toulouse (IMFT), Université de Toulouse, CNRS, 31400 Toulouse, France

Subject Areas:
fluid mechanics

Keywords:
flow-induced vibration, fluid–structure interaction, bluff body, wavelet

Author for correspondence:
Jisheng Zhao
e-mail: jisheng.zhao@monash.edu

The flow-induced vibration response of a square cross-sectional cylinder with low mass and damping ratio is analysed using continuous wavelet transforms (CWT) for three representative angles of attack of the cylinder to the incoming flow. The amplitude and frequency responses over a range of flow velocities map out multiple regimes (branches) of oscillation. Analysis of the time–frequency domain for boundary regions between branches using CWT reveals intermittency at the synchronization region boundaries as well as mode competition at branch boundaries. Complementary recurrence analysis shows that periodic dynamical states are interrupted by chaotic bursts in the transition regions around the higher branch at an angle of attack of $\alpha = 20°$ (a new branch first observed by Nemes *et al.* (2012 *J. Fluid Mech.* **710**, 102–130 (doi:10.1017/jfm.2012.353))), supporting the CWT-based frequency–time analysis.

This article is part of the theme issue 'Redundancy rules: the continuous wavelet transform comes of age'.

1. Introduction

In fluid mechanics, the term fluid-induced vibrations (FIV) describes a class of flows exhibiting a coupled interaction between a flow field and a structure vibrating in response to that flow field. A few canonical examples of this type of phenomenon are vortex-induced vibrations (VIV), galloping and aero-flutter. FIV is of

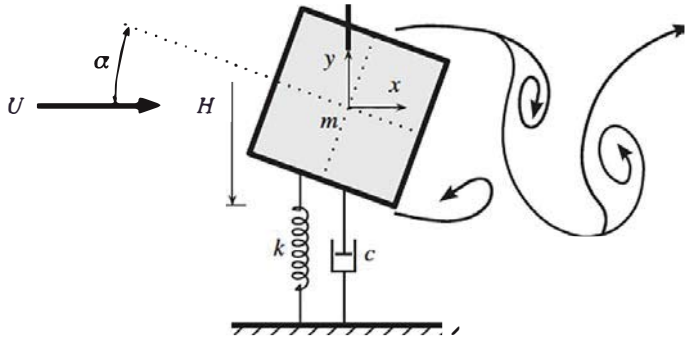

Figure 1. A definition sketch of the problem studied—a square cross section with variable angle of attack, α, constrained to oscillate across the stream.

great interest in the field of fluid–structure interaction as it has significant implications in civil and mechanical engineering, being both a potential energy harvesting source [1] and an undesirable phenomenon in practical applications [2]. In the latter case, FIV can induce cyclic fatigue on slender structures such as wind turbine towers, chimneys and oil marine risers, and can even lead to catastrophic failure such as the Tacoma Narrows Bridge collapse in 1940.

The ubiquitous nature of FIV alongside its engineering implications has motivated extensive investigations in the last half century to better characterize, model and predict its onset and response. Comprehensive reviews on this large body of research work have been given [3–5]. The types and regimes of FIV phenomena depend on (i) the mechanical and geometric properties of the structure, (ii) the flow field and fluid properties and (iii) the alignment of the flow field and the structure. The underlying model is, therefore, not only highly nonlinear in nature but also comprises an extensive number of parameters. Even simplified models, such as that of a square cross section slender body in a uniform flow, have recently [2,6] been shown to exhibit multiple vibrational modes that interact to reveal new regimes of high-amplitude vibrations.

This study follows on from [6] and investigates the flow past an elastically mounted square cross section cylinder, where the flow is perpendicular to the long axis of the cylinder, and the cylinder is constrained to oscillate across the flow (figure 1). This set-up falls under the broader class of investigations of the fluid–structure interaction of bluff, slender structures in cross-flow. This particular geometry is susceptible to two main FIV phenomena: VIV where the frequency of periodic vortex shedding and the frequency of the body oscillation synchronize; and transverse galloping, an aeroelastic instability caused by changes in the relative angle of attack induced by the body motion resulting in aerodynamic forces in the same direction as the motion [4].

The FIV of an elastically mounted body constrained to oscillate across the stream depends on the body mass in oscillation, m, the structural damping, c, and the spring stiffness, k (both assumed here to be constant), the fluid density, ρ, the kinematic viscosity, ν, and the inflow speed, U. A number of dimensionless groups can be defined, but typically for VIV studies the independent parameters used are: the mass ratio, $m^* = m/m_d$, where m_d is the mass of the fluid displaced by the body; the structural damping ratio with consideration of the added mass, $\zeta = c/(2\sqrt{k(m+m_A)})$, in which m_A is the added mass; the reduced velocity, $U^* = U/\sqrt{k(m+m_A)}H = U/f_{nw}H$; and the Reynolds number, $Re = UH/\nu$, where H is the length of the cross section perpendicular to the flow. The displaced fluid mass is defined as $m_d = \rho CL$, where C is the geometry's cross-sectional area, and L is the length of the body immersed in the fluid. For this study, the angle of attack of the square cross section with respect to the flow, α, is also a variable. Dependent variables are non-dimensionalized by the length scale, H, and the natural frequency in water, f_{nw}.

Independently, VIV and galloping have both received considerable attention. The former, in the context of slender bodies of circular cross section, has been actively researched, leading to multiple review articles [7–9]. The primary characteristic relevant to the current study is the definition of regimes of fluid–structure interaction, referred to as branches [10,11], that occur over U^* ranges. Beginning with low flow velocity, the first branch of VIV is the initial branch, where the amplitude of oscillation increases with U^* and the oscillation is modulated due to the influence of both the body's natural frequency and the Strouhal frequency (the vortex shedding frequency of a stationary cylinder). Second is the upper branch, characterized by oscillations of large amplitude at a frequency around the body's natural frequency, which appear to be unstable and chaotic [12–14]. Third is the lower branch, consisting of periodic and stable oscillations at amplitudes around $0.6D$ (with D the cylinder diameter) and a frequency around the natural frequency of the body. The vortex shedding and body oscillation are synchronized at the same frequency. Finally, the synchronization is lost and a desynchronized regime takes over, consisting of small oscillations at a fluctuating frequency around the Strouhal frequency.

The FIV phenomenon of galloping has also received attention, investigations focusing on canonical configurations of a square cross section cylinder oriented with a flat face normal to the flow. While Den Hartog [15] first proposed a criterion for the onset of galloping of ice-covered cables, Parkinson & Smith [16] developed a very successful quasi-steady theory to predict the amplitude response of a square cylinder undergoing galloping. The theory is especially successful for relatively heavy bodies, typically when surrounded by air, where the galloping oscillation frequency is much lower than the vortex shedding frequency.

Less attention has been paid to FIV of a square cylinder with variation of angle of attack. Our recent paper [2] experimentally investigated the influence of the angle of attack of a square cylinder with low mass-damping ratio on the body's FIV response, mapping out the flow regimes as a function of α and U^*. A new, previously unreported, higher branch (HB) of amplitude response was observed over a range of angles of attack, $10^\circ < \alpha < 22.5^\circ$, where the body oscillation amplitudes are considerably higher than those seen in the upper branch associated with VIV, but with an oscillation frequency locked onto approximately half of the Strouhal frequency. A numerical study by Zhao *et al*. [17], which allowed motion in both the cross-stream and streamwise directions, saw a similar high-amplitude response regime. A recent experimental study by Zhao *et al*. [6] refined and expanded our work [2], investigating representative angles of attack where the vibrations were dominated by galloping ($\alpha = 0^\circ$), by VIV ($\alpha = 45^\circ$), and an intermediate region where the HB has been observed ($\alpha = 20^\circ$). This study investigates the same parameter range as [6], though, while the latter characterized the dynamics and wake vorticity production in the regimes across this α–U^* range, this study examines the boundary regions between regimes and those featuring intermittent behaviour in oscillations using wavelet and recurrence plots.

The following section details the experimental method. Section 3 presents the obtained experimental results and the dynamic responses of a freely vibrating square cylinder at $\alpha = 0^\circ$, 45° and 20°. Lastly, conclusions of this study are given in §4.

2. Experimental method

The experiments were conducted in the free-surface recirculating water channel of the Fluids Laboratory for Aeronautical and Industrial Research (FLAIR), Monash University. More details of this water channel facility and the experimental set-up can be found in [6].

The experimental set-up is shown in figure 2. The rigid square cylinder model used in this study was made from aluminium square cross section tubing with a side width of 24.6 mm and an immersed length of $L = 620$ mm, giving an aspect ratio range of $17.8 \leq AR = L/H \leq 25.2$ across the α range. The displaced mass of water yields a minimum achievable mass ratio of $m^* = 2.64$. Details of the air bearing system and measurement acquisitions can be found in [2]. An end conditioning platform was used to promote parallel vortex shedding. The platform height ensured that the cylinder was outside the boundary layer of the channel floor and provided a

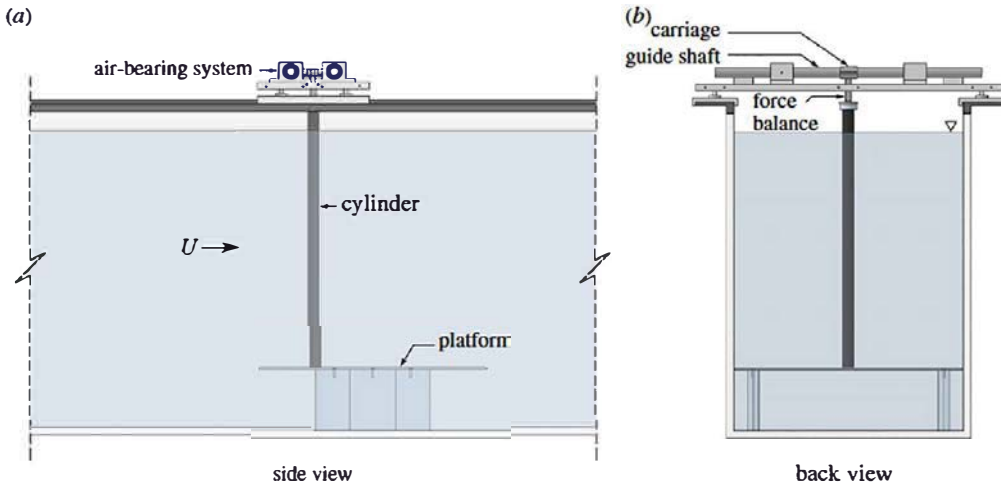

Figure 2. A schematic showing the experimental set-up in the test section of the water channel. (Online version in colour.)

gap of 1 mm between it and the cylinder free end. The natural frequencies of the system in air (assumed to be equivalent to vacuum) $f_{na} = 0.803$ Hz and water $f_{nw} = 0.648$ Hz were measured with free decay tests. The Reynolds number was varied in the range $970 < Re < 13\,460$.

To provide time-series analysis that can reveal mode competition and intermittency in the dynamical system, the body oscillations were analysed with continuous wavelet transforms (CWT) and recurrence analysis. The CWT provides temporally resolved frequency analysis to give insight into the dynamics of the vibrations through the time traces. In this study, the CWT was performed using the complex Morlet wavelet at scales $f/f_{nw} \in [0, 4]$ with the central frequency at 0.811 Hz. Recurrence analysis complements CWT by providing dynamical insight of the time series, mapping the recurrence of the system with time. This is achieved by plotting the time series onto a square matrix where the axes represent the temporal component and a Heaviside function of the L_2 norm of the phase difference for each time point to yield a symmetric binary square matrix [18].

3. Results and discussion

(a) Galloping-dominated response at $\alpha = 0°$

The classic galloping response of the square cylinder is shown in figure 3 as a function of U^* for the $\alpha = 0°$ case. Note that, in figure 3*a*, A^*_{10} represents the mean of the top 10% of the amplitude peaks normalized by H. Also shown are contours of energy as a function of frequency and U^* for the body oscillation. The normalized vibration frequency is given by $f^*_y = f_y/f_{nw}$. The contours represent the frequency power spectrum of the cylinder position time series at each measured U^* normalized by the maximum energy, and stacked horizontally to display the frequency response as a function of U^*. Three synchronization regimes were identified by Zhao *et al.* [6], where the body motion and the vortex shedding frequencies synchronized at 1 : 1, 1 : 3 and 1 : 5. These synchronization regimes were shown to have clear periodicity, with harmonic components visible for the 1 : 3 and 1 : 5 synchronization regimes observable in the total lift force and vortex lift force (see [6]).

As evident from figure 3, the first synchronization regime occurs around $U^* = 6$, where the body's vibration frequency matches the vortex shedding frequency, leading to a synchronization between the two, expected to occur when the Strouhal number $St \simeq 1/U^*$.

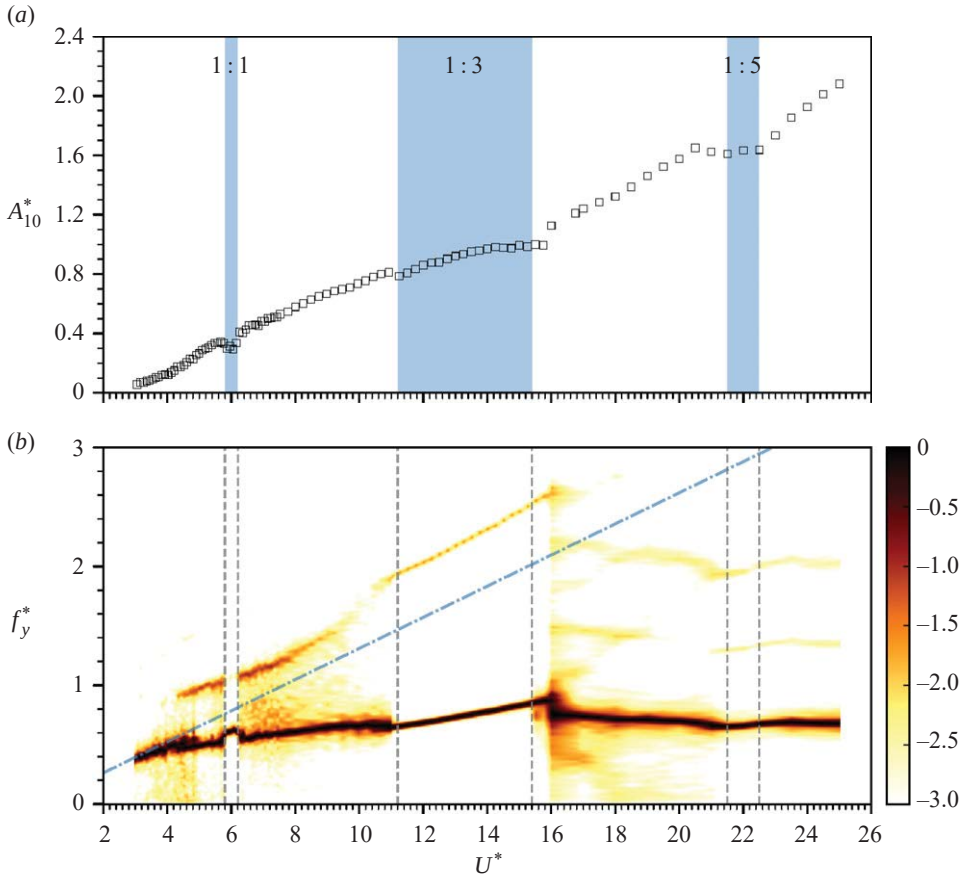

Figure 3. The normalized amplitude response and the logarithmic-scale frequency power spectral density (PSD) contours as a function of the reduced velocity for $\alpha = 0^\circ$. Note that the frequency PSD contours here are constructed by stacking the frequency PSD based on short-time Fourier transforms (STFT) at each U^* [6]. The 1 : 1, 1 : 3 and 1 : 5 synchronization regimes are highlighted with blue shading in (*a*), and their boundaries are illustrated by the vertical dashed lines in (*b*). The dotted-dashed slope line represents the Strouhal number $St \simeq 0.131$ (measured in the fixed cylinder case). (Online version in colour.)

The location of the other synchronization regimes can also be understood by considering the behaviour of the body's oscillation frequency and the vortex shedding frequency with increasing U^*. Figure 3*b* shows that over the entire range of U^* tested, the body's primary oscillation frequency f^*_y remains essentially constant. Only in the synchronization regimes does it vary noticeably, and even then only by a small amount. Figure 3 shows the synchronization regimes (1 : 1 regime over $5.8 \leq U^* \leq 6.2$, 1 : 3 regime over $11.2 \leq U^* \leq 15.4$, and 1 : 5 regime over $21.5 \leq U^* \leq 22.5$) occurring at equally spaced increments $U^* = 6$, $U^* = 14$ and $U^* = 22$ during which nonlinear synchronization causes the body's oscillation and the vortex shedding to shift from their natural values and synchronize at the values reported in figure 3.

To demonstrate the temporal evolution of the frequency content for the body vibration across these synchronization regimes, figures 4 and 5 show time series of the normalized body displacement along with the frequency energy contours based on CWT at various U^* values. At $U^* = 4.0$, where the body oscillations are non-periodic, the vibration frequency is dominated by the Strouhal frequency but with some unstable behaviour over time. As the reduced velocity is increased to $U^* = 5.0$, the body vibration appears to be more periodic, with the vibration frequency modulated by the Strouhal frequency and the natural frequency of the system. At $U^* = 6.0$, where the 1 : 1 synchronization is observed, the cylinder vibration frequency appears to be

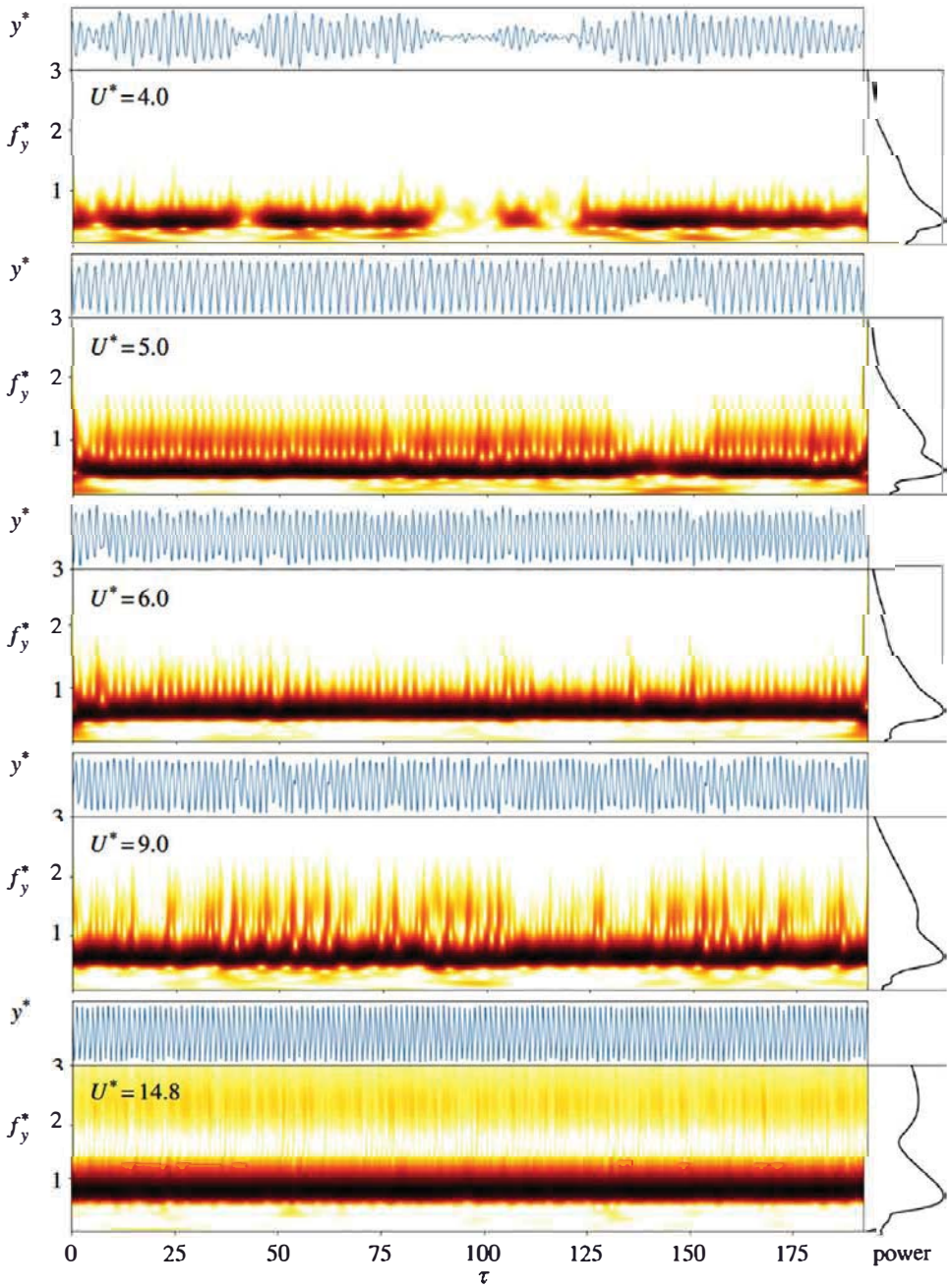

Figure 4. Time series of the normalized (measured) cylinder displacement along with the frequency energy contours based on CWT at various U^* values for $\alpha = 0°$. Note that y^* denotes the normalized body position from its neutral position at zero flow velocity; $\tau = f_{nw}t$ is the normalized time. (Online version in colour.)

stable at $f_y^* \approx 0.5$, with the influence of f_{nw} attenuated considerably; however, the periodicity is still modulated with higher-frequency components that are intermittent with relatively much weaker power. Further, at $U^* = 9.0$, located in between the 1:1 and 1:3 regimes, while the vibration frequency is dominated by a frequency lower than f_{nw}, a secondary frequency component appears intermittently with broadband noise over time. This component of higher frequency

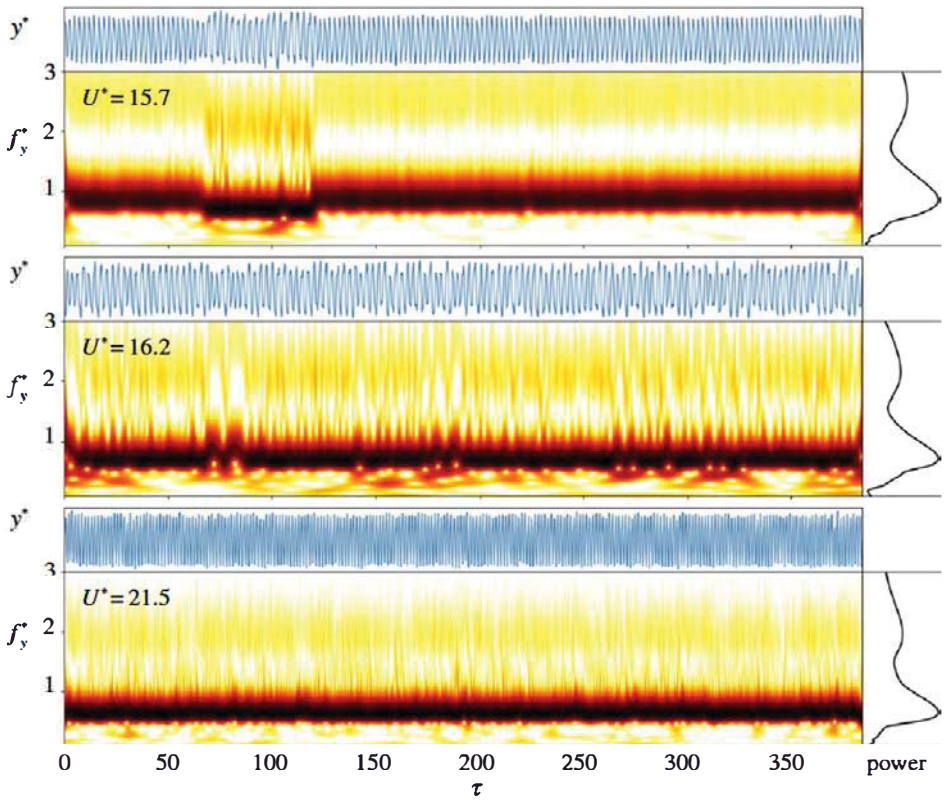

Figure 5. Time series of the normalized cylinder displacement along with the frequency energy contours based on CWT at various U^* values for $\alpha = 0°$ (continued from figure 4). (Online version in colour.)

moves towards the 1 : 3 harmonic synchronization as U^* is increased, but the combination of the vortex lift and galloping result in some aperiodic behaviour in the body oscillations, as seen in the wavelet spectra. As the reduced velocity is still further increased to $U^* = 14.8$, located in the 1 : 3 synchronization regime, the cylinder vibration is highly periodic and exhibits two components, the first and the third harmonics, with no aperiodicity or intermittency present in the synchronization range. At the end of this synchronization region, $U^* = 15.7$, the vibration frequency can be seen to contain a mode competition whereby the highly periodic 1 : 3 synchronization becomes unstable, and a lower-frequency pair with broadband noise is present as the vortex shedding and galloping forces desynchronize before regaining periodicity. At a higher reduced velocity $U^* = 16.2$, while the dominant vibration frequency remains much lower than f_{nw}, the fifth harmonic is consistently present. At this boundary region, the vortex shedding and body oscillation will intermittently 'lock' briefly, seen in the CWT as short bursts of periodicity; however, it is unstable and quickly reverts to desynchronized galloping. At $U^* = 21.5$ in the 1 : 5 synchronization region, the fundamental frequency and the fifth harmonic components become stable, resulting in stable vibration amplitudes. From the above results, the frequency–time analysis based on CWT provides an insight into the stability of the synchronization between the vibration frequency components and their behaviour over time. It also highlights that the transition regimes are sensitive to noise and can result in mode switching in boundary regions.

(b) VIV-dominated response at $\alpha = 45°$

Unlike the case at $\alpha = 0°$, the case at $\alpha = 45°$ is not susceptible to galloping. As explained by the quasi-static theory of [16], galloping should only occur when $\partial \bar{C}_y / \partial \alpha > 0°$ at the base angle of

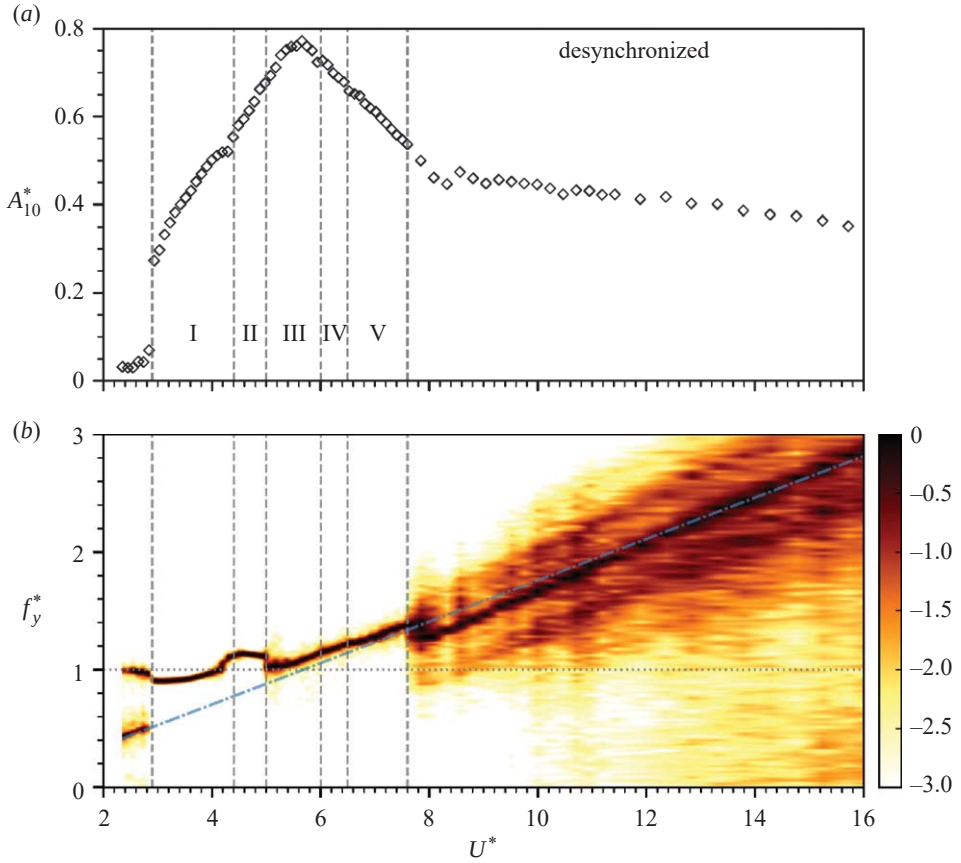

Figure 6. The amplitude and frequency responses as a function of U^* for $\alpha = 45^\circ$. Five regimes (I–V) are identified within the VIV lock-in region. In (*b*), the dotted-dashed slope line represents the Strouhal number $St \simeq 0.176$. Note that the frequency PSD contours here are constructed based on STFT analysis [6]. (Online version in colour.)

attack (here 45°), where $\bar{C}_y$ is the mean transverse lift coefficient. This does occur for $\alpha = 0^\circ$, but it does not hold for $\alpha = 45^\circ$. However, the $\alpha = 45^\circ$ case, like any bluff body that causes alternate vortex shedding, is susceptible to VIV, and this phenomenon dominates the FIV response of this case.

Figure 6 shows the variation of the amplitude of oscillation as a function of U^*, as well as the variation of the frequency content of the time–displacement series. Note that five regimes (I–V) were identified within the VIV lock region by Zhao *et al*. [6], based on an overview examination of the fluid force coefficients and the corresponding phases, and the wake mode.

It shows that the response type is quite varied, with large-amplitude oscillations for $3 < U^* < 7.5$ (the region designated as the upper branch by Nemes *et al*. [2]) consisting of five regimes, the boundaries of which are marked by the dashed vertical lines on figure 6. The characteristics of each of these regimes, as well as the initial branch and synchronization regions, are highlighted below, in order of increasing U^*.

Summarizing the regimes, for $U^* < 3$, the flow is in the initial branch as for a canonical cylinder case. The oscillations are small, comprising Strouhal and natural frequencies, resulting in a modulated response seen in the wavelet analysis in figure 7 for $U^* = 2.6$.

Between $U^* = 3$ and 4.4, the flow follows the upper branch behaviour of a circular cylinder, and the first of a series of synchronized regimes, where the vortex shedding and the body oscillation occur at the same frequency. In this first regime (I), vortex shedding occurs in the 2S mode [2,6], similar to the classic Kármán vortex street. The amplitude of oscillation in this regime is almost

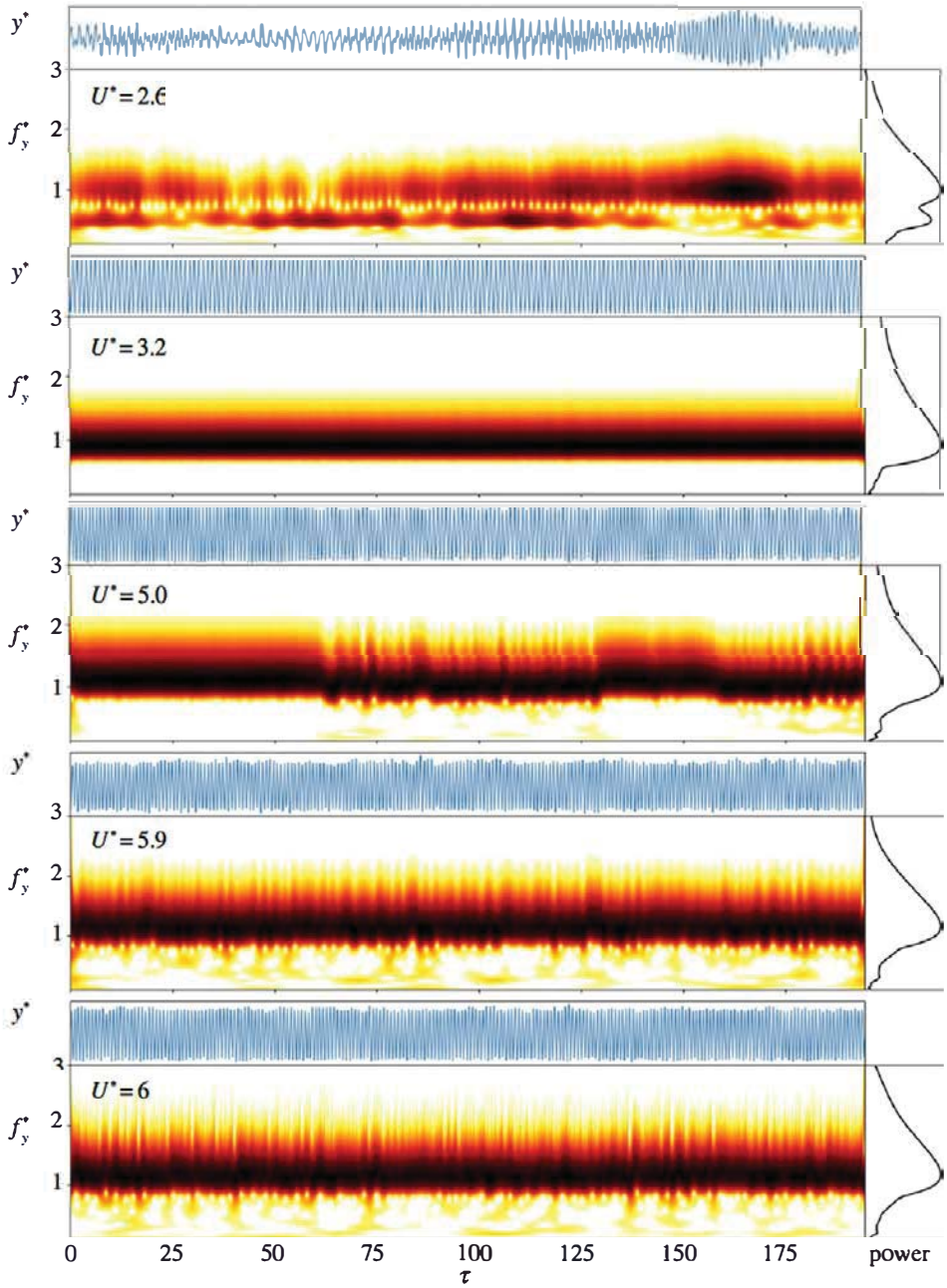

Figure 7. Time series of the normalized cylinder displacement along with the frequency energy contours based on CWT at various U^* values for $\alpha = 45°$. (Online version in colour.)

a linear function of U^*, and the frequency of oscillation is close to, but slightly below, the natural frequency of the body, with no modulation or variation in the time series ($U^* = 3.2$ in figure 7).

At $U^* = 4.4$, a change to a second distinct synchronized regime (II) occurs, observed by a small but distinct kink in the trend of amplitude as a function of U^*. There is also a distinct change in the frequency response. The frequency of oscillation and vortex shedding shifts to a value close to, but now slightly above, the natural frequency of the body. This appears to be related to a change of the added mass related to the redistribution of vorticity that occurs with the change of wake mode (see [19]).

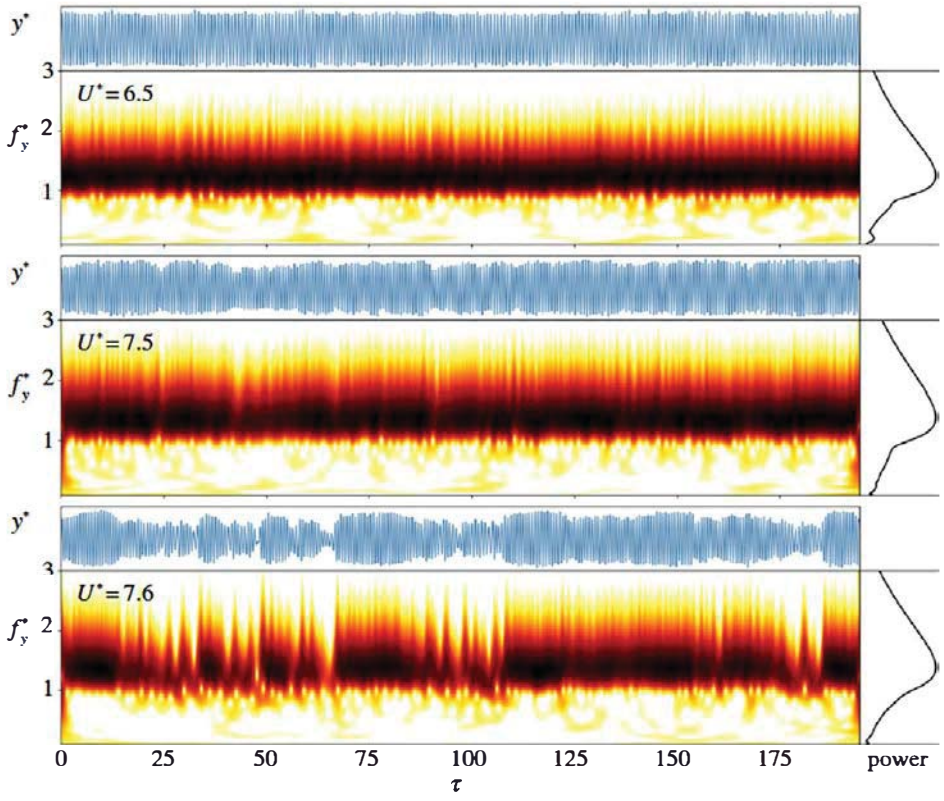

Figure 8. Time series of the normalized cylinder displacement along with the frequency energy contours based on CWT at various U^* values for $\alpha = 45°$ (continued from figure 7). (Online version in colour.)

At $U^* = 5$, there is a transition to a third distinct synchronized regime (III). The onset of this regime occurs close to the point where the body's natural frequency is equal to the Strouhal frequency. There is little discernible difference in the flow between this regime and the previous one (II); however, there is a distinct change in the oscillation response, as shown in figures 6 and 7. In the latter, a mode switching between the two responses is evident for $U^* = 5$, identified by a sudden frequency switch and modulated response in oscillation frequency occurring at $\tau \approx 60$. In the wavelet plot, the body oscillation shifts from the synchronized natural frequency to slightly above the Strouhal frequency along with an associated (small) loss of periodicity.

Figure 6 shows that the amplitude of oscillation first increases, then decreases with increasing U^* in this regime, with a peak oscillation around $U^* = 5.9$.

The reduced velocity $U^* = 6$ marks the beginning of a fourth regime (IV), distinct from the others in the high-amplitude upper branch region, as it is not periodic. Figure 6 shows that, while the frequency content of the body oscillation remains dominated by a single component at a value slightly above the Strouhal frequency, the wavelets show higher frequencies. Comparing the wavelet plot between $U^* = 5.9$ and $U^* = 6$, the oscillations appear to go from a modulated oscillation response increasing and decreasing frequency over 2–5 cycles to a higher-frequency component and less organized modulation. The cause of this response is unclear, although [6] hypothesized that it was due to the system's increased susceptibility to external noise.

Regime V begins at $U^* = 6.5$ and continues to $U^* = 7.5$, after which the body oscillation and vortex shedding become desynchronized. Like regime III, regime V consists of synchronized oscillations at a frequency slightly above the Strouhal frequency.

Finally, at $U^* = 7.5$, as shown in figure 8, the body oscillation and the vortex shedding begin to desynchronize. The vortex shedding occurs at a primary frequency close to, but slightly below,

the Strouhal frequency for the fixed body; however, the spectra are broadband, indicating that the flow is not strictly periodic. The amplitude of oscillation is only a weak negative function of U^*, as shown in figure 6. For higher U^*, there is an evident desynchronization in the time series with frequency components varying over a broadband region.

(c) Sub-harmonic VIV response at $\alpha = 20^\circ$

As demonstrated by Nemes *et al*. [2], while the case at $\alpha = 0^\circ$ is dominated by galloping response, and the case at $\alpha = 45^\circ$ is dominated by VIV response, there exists a transition between the two FIV response phenomena with variation of the angle of attack. The FIV response regime map in the U^*–α parameter space presented in [2] shows a new response regime labelled the 'higher' branch, as it is characterized by highly periodic oscillations with amplitudes larger than those present in the upper branch (UB). Later, the study of [6], by examining the representative angle of attack $\alpha = 20^\circ$, provided further details of the vibration dynamics (i.e. the structural vibration response and the fluid forcing) and revealed that a new 2(2S) wake mode was associated with a sub-harmonic synchronization in the HB. This section presents a follow-up analysis using CWT to gain a proper understanding of the temporal behaviour of the frequency response in various response regimes for the case of $\alpha = 20^\circ$. Also, a recurrence analysis is given to shed light on dynamical states of the structural vibration.

Figure 9 shows the amplitude and frequency responses as a function of U^* for the $\alpha = 20^\circ$ case. As can be seen, five response regimes are identifiable: an initial branch (IB), a UB, a HB, and two desynchronization regions. Similar to the response typical of VIV, an initial branch is encountered for low reduced velocities (i.e. $U^* < 4.2$), where the body's oscillation is characterized by low amplitudes with the oscillation frequency modulated by the Strouhal frequency and f_{nw}. The UB and HB regimes, where the body oscillations are highly periodic, occur over the reduced velocity ranges $4.4 \leq U^* \leq 6.4$ and $7.9 \leq U^* \leq 9.4$, which are highlighted with blue shading. The UB regime is associated with a 1 : 1 synchronization with a 2S vortex shedding mode consisting of two single opposite-signed vortices shed per body oscillation cycle, while the HB regime is associated with a sub-harmonic synchronization (or designated by 1 : 2 synchronization hereby) with 2(2S) vortex shedding mode consisting of two cycles of two single opposite-signed vortices shed per body oscillation cycle (see [6]). Interestingly, the HB regime is bounded by two intermittency regions (IR-I and IR-II highlighted with grey shading) in transition to the desynchronization regions (DR-I and DR-II) at lower and higher reduced velocities. It should be noted that DR-I occurs unexpectedly over the range of $6.4 < U^* < 7.4$ immediately after the UB regime, which is distinctly different from the VIV response of the cases of $\alpha = 45^\circ$ and a circular cylinder. On the other hand, DR-II at high reduced velocities (i.e. $U^* > 10.3$) appears to be similar to that seen in the case of $\alpha = 45^\circ$, where the body vibration become desynchronized with the vortex shedding and the vibration frequency exhibits broadband noise around a dominant component slightly below the Strouhal frequency.

To examine the temporal behaviour of the body vibration in the response regimes, figure 10 shows time series of the normalized body displacement and its frequency content based on CWT at various reduced velocities. At $U^* = 3.1$ from the IB regime, where the body vibration frequency is modulated generally by the Strouhal frequency and f_{nw}, the frequency content appears to be unstable over time, resulting in disordered body oscillations, which is different from the cases of $\alpha = 45^\circ$ and a circular cylinder. At a higher reduced velocity $U^* = 5.1$ in the UB regime, the frequency content is clearly stable over time, with the dominant component close to $f_y^* = 1$, resulting in highly periodic body oscillations. Further, at $U^* = 7.8$ from the IR-I region, while highly periodic large-amplitude (HB) body oscillations with two harmonic frequency components (i.e. the first and second harmonics) occur for a long time period, desynchronized oscillations with much lower amplitudes are also intermittently encountered. When the HB regime is reached at $U^* = 8.0$, the harmonic components are consistently stable over time. The further higher reduced velocity case of $U^* = 10.1$ sees intermittent switching behaviour, where highly periodic

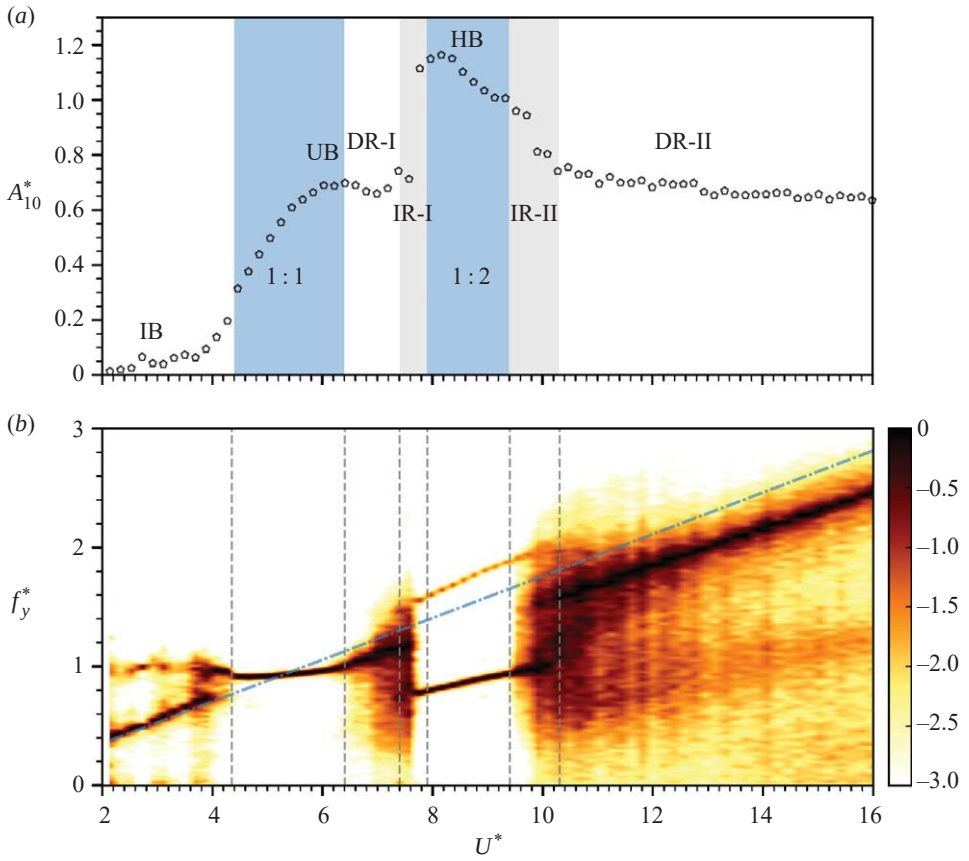

Figure 9. The amplitude response and the logarithmic-scale frequency PSD contours as a function of the reduced velocity for the case of $\alpha = 20^\circ$. The 1 : 1 and 1 : 2 synchronization regimes are highlighted with blue shading in (*a*). Two intermittency regions (IR-I and IR-II) are highlighted with grey shading. In (*b*), the vertical dashed lines illustrate the boundaries of the regimes. The dotted-dashed line represents the Strouhal number $St \simeq 0.176$. Note that the frequency PSD contours here are constructed based on STFT analysis [6]. (Online version in colour.)

oscillations are interrupted by oscillations of disorder, which is indicative of a transition to the desynchronization regime at high reduced velocity.

To further demonstrate how the dynamical state of the body vibration behaves across the regimes of interest from the UB regime to the IR-II region, figure 11 presents the corresponding *recurrence plots* (RPs) based on the body displacement signal for the selected representative U^* values. Recurrence plots were first introduced by Eckmann *et al*. [18] to visually analyse recurring patterns in time series of dynamical systems. As then, they have been employed to identify chaos in nonlinear dynamical systems in a large variety of scientific areas, from physics, to finance and economics, and to biological systems. The theory and construction method of RPs used for the present study can be found in [20]. As illustrated in figure 11*a*, for the case of $U^* = 5.1$ from the UB regime, where the body vibration is highly periodic, the RP is characterized by diagonal oriented periodic chequerboard structures. These structures are symmetric about the main (45°) diagonal (also known as the line of identity (LOI)). According to [20], the equally spaced diagonal lines parallel to the LOI are indicative of highly periodic recurrent dynamics with a single dominant frequency, noting that the horizontal distance between two consecutive diagonal lines depicts the vibration period. For the $U^* = 7.8$ from the IR-I region (figure 11*b*), periodic recurring patterns are present for $300 < \tau < 315$; however, the diagonal lines become slightly curvy, indicating that the evolution of the dynamical states is similar but at different rates (e.g. with multiple

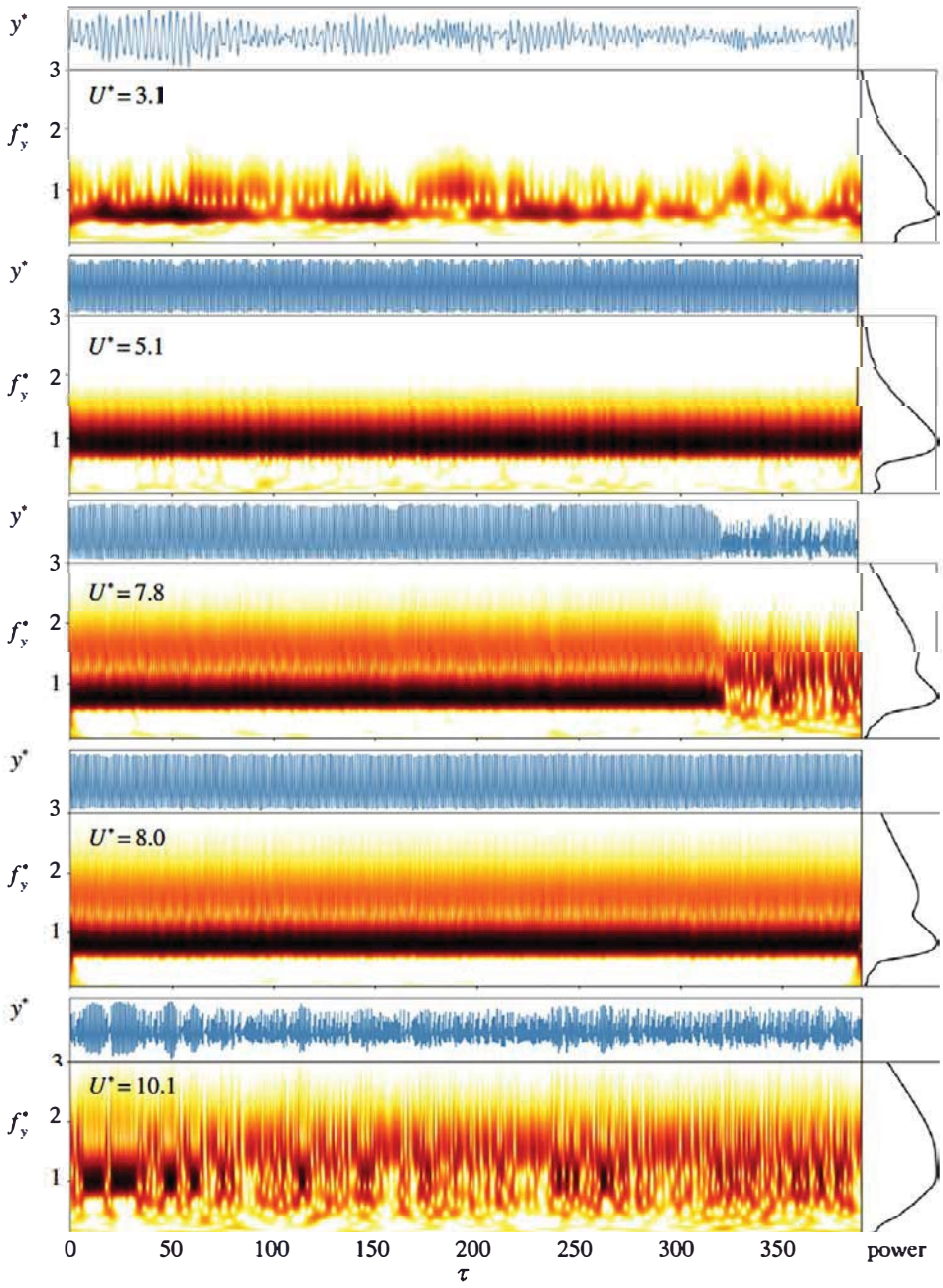

Figure 10. Time series of the normalized cylinder displacement along with the frequency energy contours based on CWT at various U^* values for $\alpha = 20°$. (Online version in colour.)

frequency components). Further, around $\tau = 320$, they exhibit some isolated black dots (with varying sizes), which are attributed to the chaotic bursts. As the system evolves further, the RP sees some horizontal curved lines and their mirrored counterparts for $\tau > 320$, indicating that some states do not change or change slowly for some time. For the $U^* = 8.0$ case from the HB regime, the RP exhibits highly periodic patterns with curved diagonal lines, indicating the existence of harmonic frequencies. Finally, for the $U^* = 10.1$ case, the RP corresponding to the IR-II region is characterized by periodic patterns intermittently interrupted by chaotic bursts (e.g.

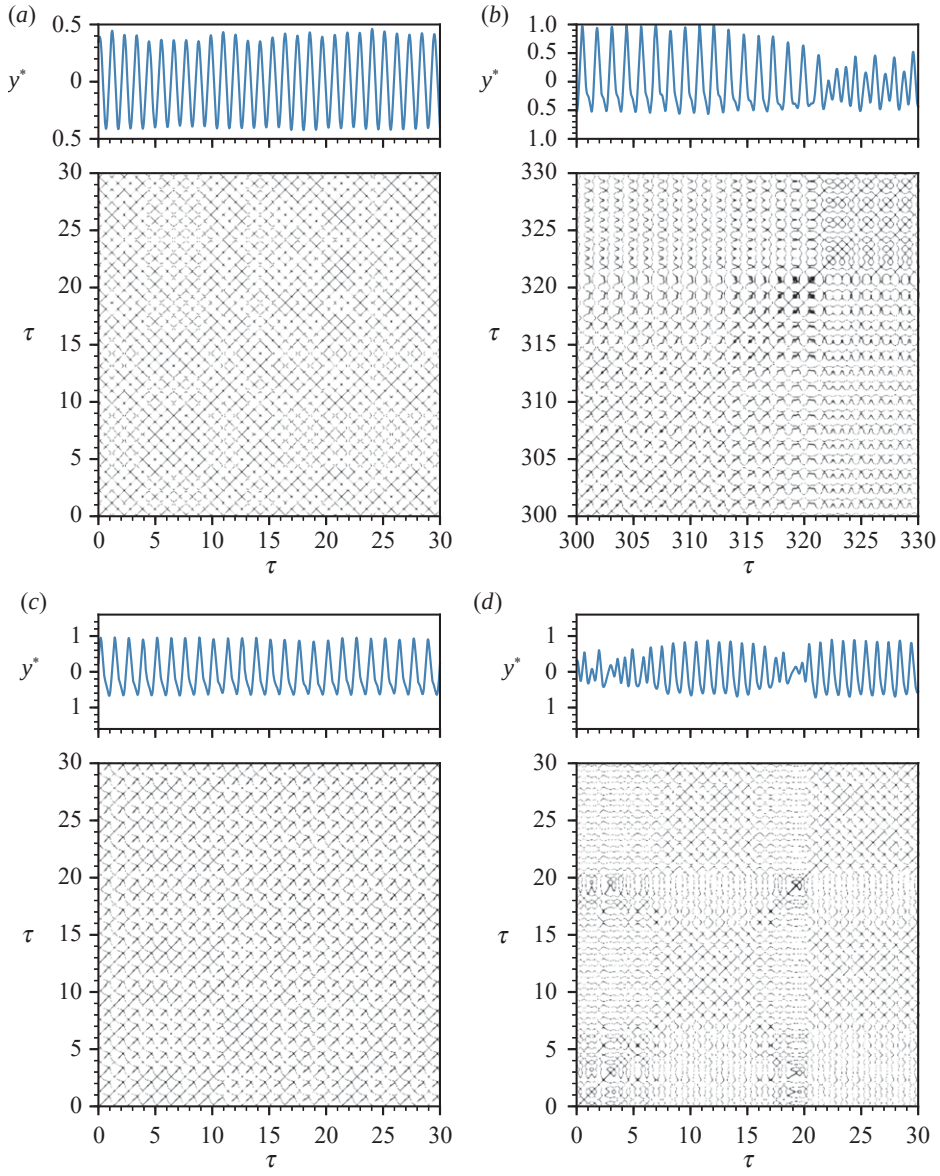

Figure 11. Recurrence plots (lower) of the time series of the normalized body displacement (upper) for the case of $\alpha = 20^\circ$ showing different dynamical states in different response regimes: (*a*) periodic state at $U^* = 5.1$ (UB), (*b*) periodic and transient chaotic states at $U^* = 7.8$ (IR-I), (*c*) periodic state at $U^* = 8.0$ (HB) and (*d*) periodic and transient chaotic states at $U^* = 10.1$ (IR-II). (Online version in colour.)

around $\tau = 20$). The above RPs show that there exist transient chaos and abrupt changes in the intermittency region IR-I and IR-II, which are consistent with the analysis using CWT.

4. Conclusion

This paper presents a CWT-based analysis of time series of the FIV of a square cross section cylinder at three representative angles of attack, $\alpha = 0^\circ$, 45° and 20°. These are associated with different mechanisms of fluid–structure interaction. The use of the CWT technique provides an insight into the temporal evolution of the frequency content, and reveals the intermittency

behaviour and transitions of the FIV response regimes for the three α cases. For the $\alpha = 0^\circ$ case that exhibits a classic galloping response, highly periodic body oscillations and stable dynamics were encountered in the 1 : 1, 1 : 3 and 1 : 5 synchronization regions over the U^* range investigated. At the boundary of these regions the time series exhibits intermittent switching of the syncrhonization. For the $\alpha = 45^\circ$ case, which exhibited a VIV-dominated response, the CWT analysis reveals intermittent mode competition in the body oscillation time trace throughout the synchronization region at the branch boundary values. Finally, for the $\alpha = 20^\circ$ case of asymmetric orientation, intermittent vibration and competition appeared in the initial branch ($U^* < 4.2$). As U^* was increased to the upper branch regime (over $4.4 \leq U^* \leq 6.4$) associated with a 1 : 1 synchronization, highly periodic body vibration was observed with stable dynamics over time. Stable dynamics was also found in the high branch associated with a 1 : 2 sub-harmonic synchronization. Outside the HB regime, the periodic body oscillations contain intermittency, IR-I and IR-II, and a transition to two subsequent desynchronization regions. Complementary recurrence plots show that periodic states are interrupted by chaotic bursts in the IR-I and IR-II regions.

Data accessibility. The datasets supporting this article have been uploaded to the online repository https://doi.org/10.6084/m9.figshare.5991232 [21].

Authors' contributions. J.Z. designed and performed the experiments, participated in data analysis and drafted the manuscript. A.N. participated in data analysis and drafted the manuscript. D.L.J. and J.S. participated in data analysis and reviewed the manuscript. All the authors gave their final approval for publication.

Competing interests. We declare we have no competing interests.

Funding. The financial support from Australian Research Council Discovery Project grant no. DP110102141 and the Centre National de la Recherche Scientifique (CNRS) grant no. PICS161793 (under the Projet International de Coopération Scientifique) is gratefully acknowledged.

Acknowledgements. The authors thank Nat DeRose, Mark Symonds and Hugh Venables for their help in the construction of the experimental apparatus.

References

1. Wang Z, Du L, Zhao J, Sun X. 2017 Structural response and energy extraction of a fully passive flapping foil. *J. Fluids Struct.* **72**, 96–113. (doi:10.1016/j.jfluidstructs.2017.05.002)
2. Nemes A, Zhao J, Lo Jacono D, Sheridan J. 2012 The interaction between flow-induced vibration mechanisms of a square cylinder with varying angles of attack. *J. Fluid Mech.* **710**, 102–130. (doi:10.1017/jfm.2012.353)
3. Blevins RD 1990 *Flow-induced vibration*, 2nd edn. Malabar, FL: Krieger.
4. Naudascher E, Rockwell D. 2005 *Flow-induced vibrations: an engineering guide*. New York, NY: Dover.
5. Païdoussis MP, Price S, De Langre E. 2010 *Fluid–structure interactions: cross-flow-induced instabilities*. Cambridge, UK: Cambridge University Press.
6. Zhao J, Leontini JS, Lo Jacono D, Sheridan J. 2014 Fluid–structure interaction of a square cylinder at different angles of attack. *J. Fluid Mech.* **747**, 688–721. (doi:10.1017/jfm.2014.167)
7. Bearman PW. 1984 Vortex shedding from oscillating bluff bodies. *Annu. Rev. Fluid Mech.* **16**, 195–222. (doi:10.1146/annurev.fl.16.010184.001211)
8. Sarpkaya T. 2004 A critical review of the intrinsic nature of vortex-induced vibrations. *J. Fluids Struct.* **19**, 389–447. (doi:10.1016/j.jfluidstructs.2004.02.005)
9. Williamson CHK, Govardhan R. 2004 Vortex-induced vibration. *Annu. Rev. Fluid Mech.* **36**, 413–455. (doi:10.1146/annurev.fluid.36.050802.122128)
10. Khalak A, Williamson CHK. 1996 Dynamics of a hydroelastic cylinder with very low mass and damping. *J. Fluids Struct.* **10**, 455–472. (doi:10.1006/jfls.1996.0031)
11. Govardhan R, Williamson CHK. 2000 Modes of vortex formation and frequency response of a freely vibrating cylinder. *J. Fluid Mech.* **420**, 85–130. (doi:10.1017/S0022112000001233)
12. Hover FS, Techet AH, Triantafyllou MS. 1998 Forces on oscillating uniform and tapered cylinders in crossflow. *J. Fluid Mech.* **363**, 97–114. (doi:10.1017/S0022112098001074)
13. Morse TL, Williamson CHK. 2009 Prediction of vortex-induced vibration response by employing controlled motion. *J. Fluid Mech.* **634**, 5–39. (doi:10.1017/S0022112009990516)

14. Zhao J, Leontini JS, Lo Jacono D, Sheridan J. 2014 Chaotic vortex induced vibrations. *Phys. Fluids* **26**, 121702. (doi:10.1063/1.4904975)
15. Den Hartog JP. 1932 Transmission line vibration due to sleet. *Trans. Am. Inst. Electr. Eng.* **51**, 1074–1076. (doi:10.1109/T-AIEE.1932.5056223)
16. Parkinson GV, Smith JD. 1964 The square prism as an aeroelastic non-linear oscillator. *Q. J. Mech. Appl. Math.* **17**, 225–239. (doi:10.1093/qjmam/17.2.225)
17. Zhao M, Cheng L, Zhou T. 2013 Numerical simulation of vortex-induced vibration of a square cylinder at low Reynolds number. *Phys. Fluids* **25**, 023603. (doi:10.1063/1.4792351)
18. Eckmann J, Kamphorst SO, Ruelle D. 1987 Recurrence plots of dynamical systems. *Europhys. Lett.* **4**, 973. (doi:10.1209/0295-5075/4/9/004)
19. Lighthill J. 1986 Fundamentals concerning wave loading on offshore structures. *J. Fluid Mech.* **173**, 667–681. (doi:10.1017/S0022112086001313)
20. Marwan N, Romano MC, Thiel M, Kurths J. 2007 Recurrence plots for the analysis of complex systems. *Phys. Rep.* **438**, 237–329. (doi:10.1016/j.physrep.2006.11.001)
21. Zhao J, Nemes A, Lo Jacono D, Sheridan J. 2018 Branch/mode competition in the flow-induced vibration of a square cylinder. Dryad Digital Repository. (doi:10.6084/m9.figshare.5991232)